THE ELECTRODEPOSITION OF COBALT SULFIDE/MOLYBDENUM SULFIDE HETEROSTRUCTURES FOR HER IN ACIDIC AND ALKALINE SOLUTIONS AND THE GROWTH OF MOS_2 NANOWIRE CATALYSTS TO ENABLE LONG-TERM HUMAN ACTIVITY ON MARS

Lee Kendall[1], Dawn Ford[2], Qiyuan Lin[1], Giovanni Zangari[1], Stephen McDonnell[1]

[1]Department of Materials Science and Engineering, University of Virginia, 395 McCormick Road, Charlottesville, VA 22903, United States

[2]Department of Physics, University of Virginia, 382 McCormick Road, Charlottesville, VA 22903, United States

Abstract

MoS_2 has attracted significant attention as a non-platinum group electrocatalyst for the hydrogen evolution reaction (HER). There have been extensive efforts demonstrating that by doping MoS_2 with various transition metals, such as Co, the HER activity of the catalyst is enhanced. Additionally, work has shown that various cobalt sulfide phases can act as a co-catalyst with MoS_2. Here, we report on the electrodeposition of a CoS_x/MoS_2 heterostructure catalyst for the HER reaction in both acidic and alkaline conditions. The most promising catalyst composition demonstrated excellent stability in both acidic and alkaline conditions with low overpotentials to reach 10 mA/cm^2 of 112 mV and 60 mV and with Tafel slopes of 113 mV/dec and 81 mV/dec, respectively. This demonstrates that the CoS_x/MoS_2 heterostructure is one of the most catalytically active materials for HER, especially in alkaline conditions. Another promising route to increasing the catalytic activity of MoS_2 is to increase the number of catalytically active edge sites. To accomplish this, ZnO nanowires are grown to act as a scaffolding for the electrodeposition and annealing of MoS_2 nanowires. By investigating different growth conditions, we are able to control the subsequent morphology and have begun tailoring the properties of the MoS_2 nanowires.

Introduction

This work was motivated by the need to develop extremely robust and effective methods for extending human activity on Mars due to the increasing drive to further explore and eventually send humans to Mars[1]. As the surface of Mars is unsuitable for extended human activity, future explorations will require a steady source of oxygen and energy, both for daily needs as well as for returning to Earth. Among technologies available on Mars, solar energy is by far the largest available resource[2]. Additionally, as the global demand for energy consumption increases, there will be a need to transition away from conventional energy sources. To meet these demands while also mitigating contributions to irreversible climate change, there is a need for sustainable and renewable energy sources.[3] One such technology is the generation of hydrogen via water splitting as it is a sustainable, secure, and clean alternative energy carrier[4]. However, to facilitate and fully realize this technology, catalysts with sufficient catalytic activity, efficiency, low-cost, and environmentally friendly materials must be developed. [5–7] Among the most active and best catalysts are noble metals, such as platinum, however their use is limited due to their scarcity and cost. [5,8]

In this context, alternative catalysts based on naturally abundant materials, such as

transition metal sulfides, phosphides, nitrides, and carbides are being strongly pursued.[9,10,19–21,11–18] One prominent example is MoS_2, an electrocatalyst that features a small Gibbs adsorption energy for H^+, $\Delta G^H_{0,ads}$, which correlates to the ability to facilitate the hydrogen evolution reaction (HER).[22–27] However, this low $\Delta G^H_{0,ads}$ is only observed along the edge planes of the crystalline MoS_2, thereby limiting the density of catalytically active sites. Recent efforts have attempted to increase the number of active sites in MoS_2 and other transition metal dichalcogenides via several approaches such as: vertically aligned synthesis, the creation of sulfur vacancies, or heteroatom doping.[26,27,36–39,28–35]

In recent years, great attention has been given to other transition metal sulfides, such as Co, Ni, and Fe. Among the most successful have been those of Co sulfides, showing strong electrocatalytic activity towards HER in both acidic and alkaline conditions.[40–43] Bonde et al. demonstrated that doping Co-atoms on the edges of MoS_2 greatly enhanced the HER activity, owed to the decrease of adsorption energy of hydrogen.[44] Another example showed the synergistic effect between Co_9S_8 and MoS_2 towards HER in alkaline environments.[45] Finally it has been shown that the interface between cobalt sulfides and molybdenum sulfide is critical to the HER performance because the formation of nano-interfaces facilitates enhanced charge transfer between Co and Mo through S-linkage.[46]

Many catalysts for HER require a polymer binder to anchor the catalyst to the working electrode, increasing resistance and hindering active sites. Therefore, direct growth of the catalyst on the current collector can increase the HER performance of the catalyst towards HER. Carbon paper exhibits high conductivity, good mechanical strength, inexpensive, and is flexible, making it an excellent candidate for the substrate. In addition, carbon paper is a porous material with a three-dimensional morphology, allowing more active sites per unit area. It also facilitates the growth of nanowires structures. Additionally, it has been shown that MoS_2 on carbon paper provides higher catalytic activity when compared to a traditional flat substrate.[47–49]

Herein, heterostructures CoS_x-MoS_2 were synthesized via a facile one electrolyte electrodeposition process followed by a simple annealing process. Several compositions were tested to elucidate the optimal conditions, as well as determine the underlying factors that influence the overall HER properties. As prepared CoS_x-MoS_2 electrocatalysts formed various morphologies, such as platelets, clusters, and nanostrips, and crystal structures depending on the synthesis conditions and therefore exhibited drastically different HER properties. Overall, the highest performing catalysts exhibited excellent electrocatalytic activity towards HER in both acidic and alkaline environments, only requiring 112 mV and 60 mV respectively to reach 10 mA/cm^2. Together, these results highlight the synergistic effects among various cobalt sulfide species and MoS_2 towards HER.

In conjunction with the growth of CoS_x/MoS_2 heterostructures on carbon paper, ZnO nanowires can also be grown on carbon paper and can act as a sacrificial scaffolding for the growth of MoS_2 nanowires. Through an investigation in the processing conditions, such as annealing temperature and subsequent etching procedures, we are able to control the composition and morphology of the MoS_2 nanowires.

Experimental

Electrolyte Preparation

The Co-Mo sulfide catalysts were electrodeposited from an electrolyte containing precursors of Co, Mo, and S. The electrolyte was prepared from cobalt nitrate hexahydrate ($Co(NO_3)_2 \cdot 6H_2O$), sodium molybdate dihydrate ($Na_2MoO_4 \cdot 2H_2O$), and thiourea (CH_4N_2S). The sodium molybdate dihydrate concentration was held at 75 mM and the thiourea concentration was held at 0.2 M while the cobalt nitrate hexahydrate concentration was varied from 5 mM up to 100 mM. Samples will be referred by their Co – Mo precursor concentrations in mM, e.g., 25-75 will be in reference to 25 mM $Co(NO_3)_2 \cdot 6\ H_2O$ – 75 mM $Na_2MoO_4 \cdot 2H_2O$.

Sample ID	$Co(NO_3)_2$ Precursor Concentration	Na_2MoO_4 Precursor Concentration
5-75	5 mM	75 mM
15-75	15 mM	75 mM
25-75	25 mM	75 mM
50-75	50 mM	75 mM
75-75	75 mM	75 mM
100-75	100 mM	75 mM

The molybdenum disulfide was electrodeposited from a chemical bath containing precursors of Mo^{6+} and S^{2-} ions, based on Levinas et al. preparation[50]. In short, the electrolyte was prepared from sodium molybdate dihydrate ($Na_2MoO_4*2H_2O$) and sodium sulfide hydrate (Na_2S*H_2O) were mixed in a ratio of Mo/S = 1/4 with molarities of 50 mM and 0.2 M, respectively.

The initial pH of the solution was approximately 13 and was acidified using sulfuric acid to a pH of 8.

Electrodeposition

All electrochemical deposition was carried out using a G&G PAR Model 273A potentiostat in a standard three-electrode setup containing a graphite rod as a counter electrode and saturated Hg/Hg_2SO_4 (MSE) as the reference electrode. The substrate was binder free carbon paper and acted as the working electrode.

Post-Synthesis Processing

To crystallize the samples, annealing was carried out in an MTI OTF-1200X tube furnace. Annealing was performed by heating the CoS_x/MoS_2 samples to 450°C at a ramp rate of 14°C/minute and a variety of temperatures for the MoS_2 nanowires where they were each held for 60 minutes before being naturally cooled back to ambient temperature. All anneals took place in the presence of flowing forming gas (5% H_2 / 95% Ar) with 3 grams of elemental sulfur upstream of the substrate. Prior to the anneal, the chamber was purged with excess forming gas for 45 minutes to minimize the presence of any impurities within the furnace. Natural cooling was carried out under the forming gas prior to the samples being removed from the furnace.

Electrochemical Characterization

Electrochemical characterization of the prepared films for HER was performed by a three-electrode configuration using a BioLogic SP-150 potentiostat. The Co-Mo sulfide/MoS_2 nanowires, graphite rod, and Ag/AgCl were used as the working, counter, and reference electrode, respectively. All experiments were carried out at room temperature and in fresh 0.5 M H_2SO_4 for the acidic conditions and fresh 1 M KOH for the alkaline conditions. The electrochemical potential difference between the reversible hydrogen electrode (RHE) and the reference electrode is given by E(RHE) = E(Ag/AgCl) + 0.197 V. All potentials were iR-compensated to 85% with the built-in program. The polarization curves of HER were measured

using linear sweep voltammetry (LSV) at a starting potential of open circuit potential and swept at a rate of 10 mV/sec with a cutoff current density of 40 mA/cm^2. The shown LSV data is after 10 sweeps unless otherwise stated.

Materials Characterization

Raman spectroscopy was collected using a Renishaw Raman instrument with a 514 nm laser excitation, 1800 grating, 20x objective magnification. X-ray diffraction was collected with a Malvern-Panalytical Empyrean diffractometer with a Cu anode (1.54 Å wavelength) in a Bragg-Brentano geometry with a reflection-transmission spinner sample holder. X-ray photoelectron spectroscopy (XPS) spectra were collected from a Scienta Omicron R3000 using monochromatic Al Kα emission with an excitation energy of 1486.7 eV and a pass energy of 50 eV. SEM was taken on a FEI Quanta 650 Scanning Electron Microscope in secondary electron mode with an accelerating voltage of 15.00 kV and a spot size of 3.0.

Results and Discussion – CoS_x/MoS_2 Catalysts for HER

To understand the structural and morphological features of the catalysts, SEM images were collected. Slow magnification image shows uniform coverage of the carbon paper substrate. The lower Co:Mo ratio samples showed less coverage of the carbon paper, notable 5-75, due to the difficulty in depositing only Molybdenum[51]. The high magnification SEM images revealed that the morphology drastically changed depending on the concentration ratio of the Co and Mo precursors as seen in Figure 1. In the sample with the lowest Co concentration, 5-75, thin sheets with small clusters are observed along the edges. When the Co was increased to 15-75, the sheets are no longer observed, and instead large plate-like structures are formed showing clustering on the surface. In the 25-75 sample, the plates grew, however the surface was largely featureless and little clustering was observed. The morphology continued to change in 50-75 as the large plate like

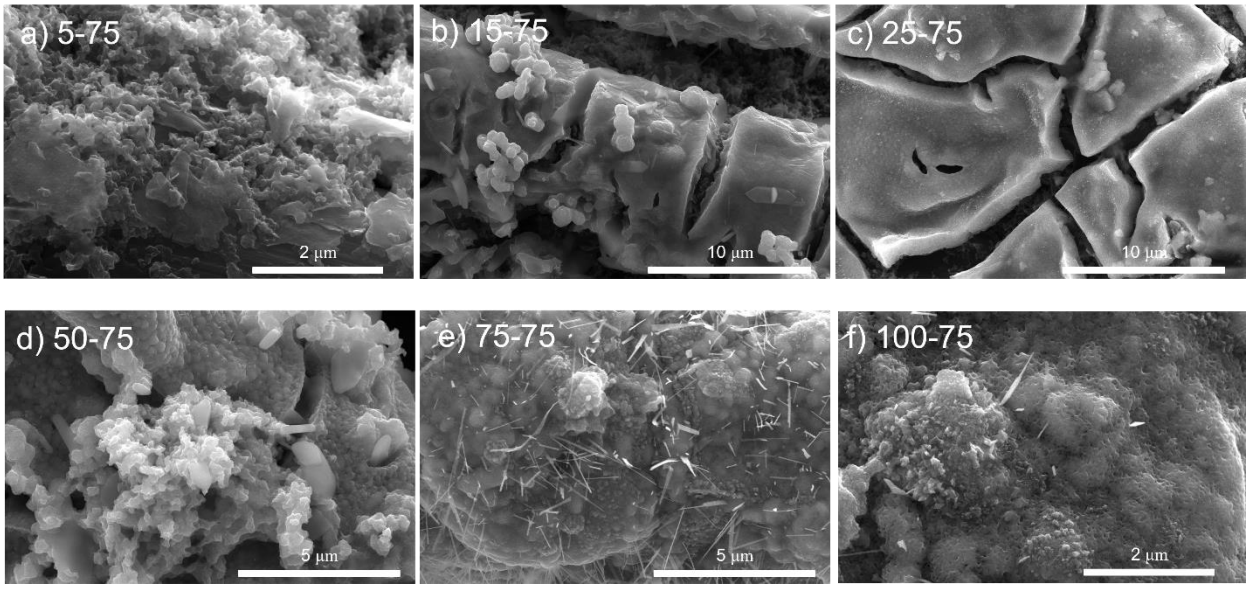

Figure 1: SEM images of a) 5-75, b) 15-75, c) 25-75, d) 50-75, e) 75-75, and f) 100-75

structures are no longer observed and instead a much rougher, scaled surface is formed with clusters of sheets on the surface. The 75-75 sample lacked the scaled surface and instead exhibited round, textured structures with long, flat, and wide features protruding perpendicular to the surface. Finally, the 100-75 sample is even more textured than 75-75 and lacks the flat sheets protruding from the surface.

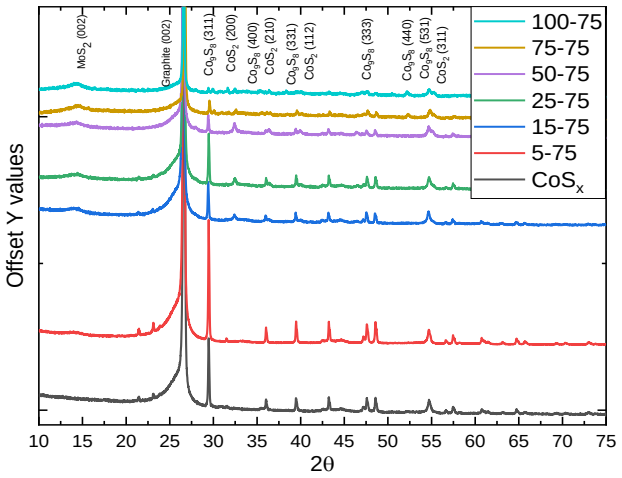

Figure 2: XRD pattern of the various catalysts

XRD patterns shown in Figure 2 provide crystallographic information on the catalysts. The Bragg diffraction hump located at $2\theta \approx 14.5°$ was indexed to the (002) plane of hexagonal MoS_2.[52] The peaks located at $2\theta \approx$ 29.5, 39.4, and 47.5° are indexed as the (311), (331), and (333) planes of cubic Co_9S_8 respectively.[53] The diffraction peaks associated with the (200) and (210) planes of cubic CoS_2 were observed at $2\theta \approx 32.4$, and 36.3° respectively.[54] It is noticed that the MoS_2 (002) diffraction peak increases in intensity as the Co concentration increases. This increase in MoS_2 is being attributed to the co-deposition of Mo with Co, in which the Co induces more Mo to be deposited during the electrodeposition process, as the redox potential of Mo is quite large and no Mo would be deposited without the co-deposition.[51] Additionally, the diffraction peaks decrease in intensity and sharpness as the Co concentration increases, indicating that the crystallite size is decreasing. As the Co precursor concentration increases, the diffraction peaks associated with Co_9S_8 decrease in relative intensity while the diffraction peaks associated with CoS_2 increase in relative intensity.

To further elucidate the crystalline structure of the grown materials, Raman spectroscopy was performed on all materials as shown in Figure 3. The peaks at roughly 384 cm^{-1} and 407 cm^{-1} are attributed to the in-plane E_{2g} mode and the out-of-plane A_{1g} mode, respectively.[55] The peaks at 289 cm^{-1}, 318 cm^{-1}, and 393 cm^{-1} are ascribed to the E_g, $T_g(1)$, and A_g modes of CoS_2 with the shoulder at roughly 418 cm^{-1} the $T_g(2)$ mode.[56] The peak found at 680 cm^{-1} is attributed to the primary vibration mode of Co_9S_8.[57] The primary peaks for the different species are labelled with a dashed line in Figure 3. In the CoS_x sample, both peaks associated with CoS_2 and Co_9S_8 are present. However, when in the presence of Mo species, the Co_9S_8 vibration modes are extinguished and are not seen at any Co/Mo ratio. At low Co/Mo ratio, as in 5-75 and 15-75, the MoS_2 features dominate the spectra. As the Co/Mo ratio

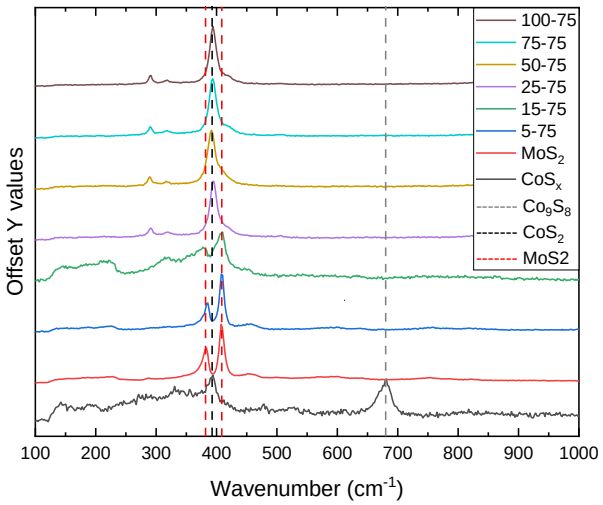

Figure 3: Raman spectroscopy of the various catalysts

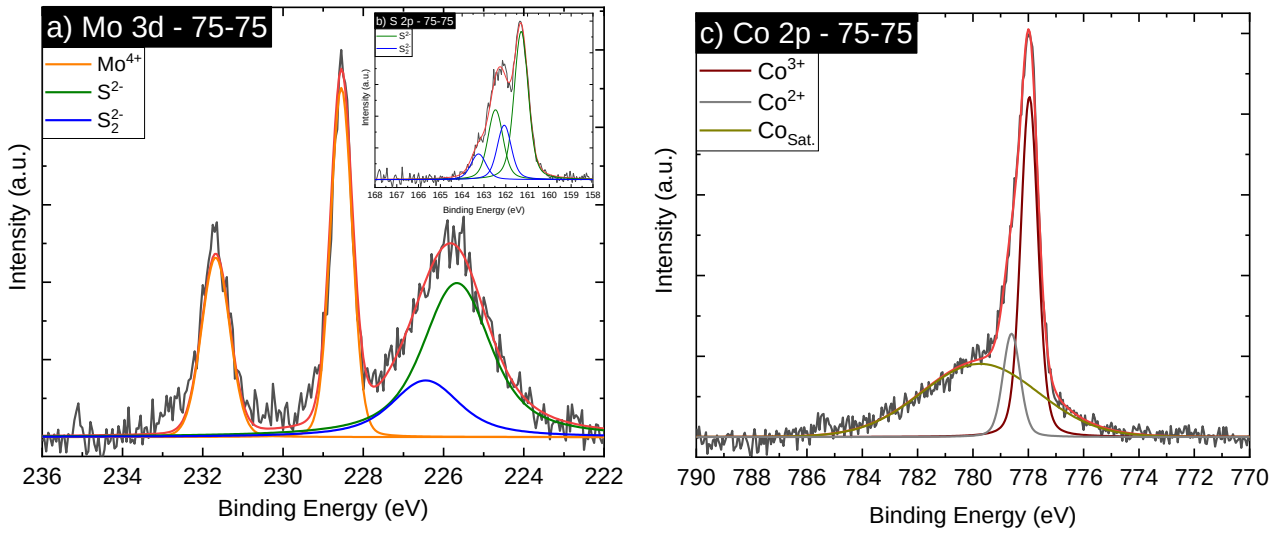

Figure 4: Deconvoluted XPS Spectra of a) the Mo 3d, b) S 2p, and c) Co $2p_{3/2}$

increases to 25-75 and beyond, the CoS_2 features dominate the spectra.

To give elemental and chemical composition of the 75-75 catalyst, XPS was conducted, as seen in Figure 4. The Mo 3d spectra can be deconvoluted into distinctive peaks of a single double ($3d_{5/2}$ and $3d_{3/2}$) of Mo^{4+} and singlets of the various overlapping S 2s states that occur in the same energy range.[58–60] The Mo 3d peaks were deconvoluted with a binding energy difference of 3.13 eV between the $3d_{5/2}$ and $3d_{3/2}$ and with a fixed intensity ratio of 3:2. In the sulfur spectrum, the presence of S^{2-} and S_2^{2-} was detected; this is consistent with previous literature.[58,61] The sulfur spectrum was deconvoluted with two doublets, with the constraints of an energy difference of 1.18 eV between the $2p_{3/2}$ and $2p_{1/2}$ and with an intensity ratio of 2:1. The cobalt $2p_{3/2}$ spectrum was deconvoluted with two primary features at 777.96 eV, 778.6 eV corresponding to Co^{3+} and Co^{2+} respectively, and with a large satellite peak at higher binding energy.[43,62]

The impact of the Co/Mo precursor ratio on the HER properties of the catalysts in acidic conditions, polarization experiments were performed, shown in Figure 5. The overpotential required to reach the cathodic current density of 10 mA/cm^2 (η_{10}) was used to compare the catalytic activity of the HER catalysts and these are shown in the subset of Figure 5. As seen in Figure 5, the 75-75 sample performed the best by exhibiting the lowest overpotential (112 mV) to reach 10 mA/cm^2. This performance was greater than that of either CoS_x or MoS_2 and superior than that of similar cobalt sulfide-based catalysts[63]. The other values of the catalysts η_{10} can be seen in the Figure 5 subset plotted against their Co/(Co+Mo) as well as in table below.

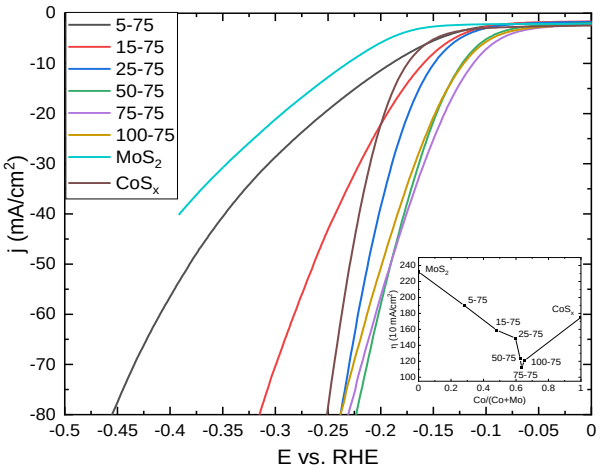

Figure 5: Polarization curves in 0.5M H_2SO_4 of the various catalysts; subset) η_{10} vs Co/(Co+Mo)

HER in alkaline medium is also of high interest due to the widespread usage of alkaline water electrolysis in industry, as well reducing the corrosion of electrolytic cells found in acidic cells. Polarizations in 1 M KOH were carried out to investigate the Co-Mo sulfide catalysts affinity towards HER in basic conditions. All but the 75-75 sample degraded quickly per scan within the alkaline medium. The subset of Figure 6 shows the degradation of the 25-25 sample as an example of the instability found in other samples. The sample 75-75 showed good stability, as can be seen in Figure 6. Additionally, 75-75 showed an extremely low η_{10} value of 60 mV, one that competes with state-of-the-art catalysts in alkaline medium[64].

The Tafel slope (b), or the slope of the linear, low overpotential regime in the Tafel plot, is the overpotential required to increase the current density by one order of magnitude. As such, it is optimal to have a catalyst with a lower Tafel slope for HER applications. The Tafel slope is dependent on the mechanistic pathway where the HER mechanism involves three known elementary reaction steps in acidic media and three known elementary reaction steps in alkaline media where the reactions are strongly dependent on the inherent surface chemistry and electronic structure of the catalyst. The Tafel slopes for the Co-Mo sulfide catalysts are listed in table below and suggest a Volmer-Heyrovsky mechanism, consistent with literature[62,65,66]

As the Raman data demonstrates, the samples with more CoS_2 like structures had the highest performance in acidic conditions compared to those with a more MoS_2 like spectra. This is to be expected as previous literature has demonstrated that cobalt sulfide based materials superior catalytic performance over crystalline MoS_2.[17,23,26,63,65–67] However, while the samples 25-75 through 100-75 have

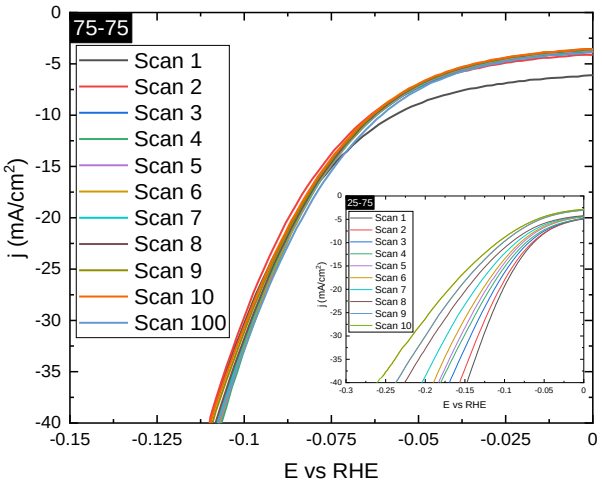

Figure 6: Polarization curves in 1 M KOH of the various catalysts; subset) example of unstable catalyst

similar Raman spectra, they have very different catalytic activities in acidic conditions and stability in alkaline conditions. Diffraction patterns of various catalysts obtained via XRD can help elucidate the origin of these performances as the XRD between the samples are quite different. At high cobalt fraction, the crystallite size of the cobalt sulfide phases decreases, allowing an increase in the concentration of linking disulfide anions, the catalytically active sites, to be exposed to the electrolyte.[68] Also, as smaller grains allow for more of these nano-interfaces, a higher density of active sites which led to an improvement of the electrocatalytic activity was observered.[46,62,69] Additionally, the increase in the MoS_2 phase with the higher Co/Mo ratios likely contributes to this increase in overall catalytic activity of the catalyst due to their synergistic properties, such as better charge transfer and facilitation of H- containing species adsorption-desorption at the active sites[62,70,71].

However, this does not directly explain the difference in stability and overall performance of 75-75 compared to the rest of the synthesized catalysts in alkaline conditions. As the only major difference in the high Co/Mo

ratio catalysts is the morphology, we suggest that this stability is related to the morphology and crystallography of the 75-75 catalyst. As seen in Figure 1, the 75-75 sample is the only catalyst to exhibit the wide, flat, and protruding features. We suggest that at low Co concentration, the stabilizing CoS_x in alkaline conditions show low concentration, as per the SEM EDS, and at high Co concentration the grains are too small and are more easily broken down due to the more accessible linking disulfide anions.[68]

Sample	Composition (Co/(Co+Mo)	Acidic η_{10} (mV)	Acidic b (mV/dec)	Alkaline η_{10} (mV)	Alkaline b (mV/dec)
5-75	0.282	190	157	Unstable	NA
15-75	0.482	159	106	Unstable	NA
25-75	0.597	149	84	Unstable	NA
50-75	0.626	123	118	Unstable	NA
75-75	0.635	112	113	60	81
100-75	0.653	121	114	Unstable	NA
MoS_2	0	232	123	Unstable	NA
CoS_x	1	175	87	Unstable	NA

Results and Discussion – Synthesis of MoS_2 Nanowires

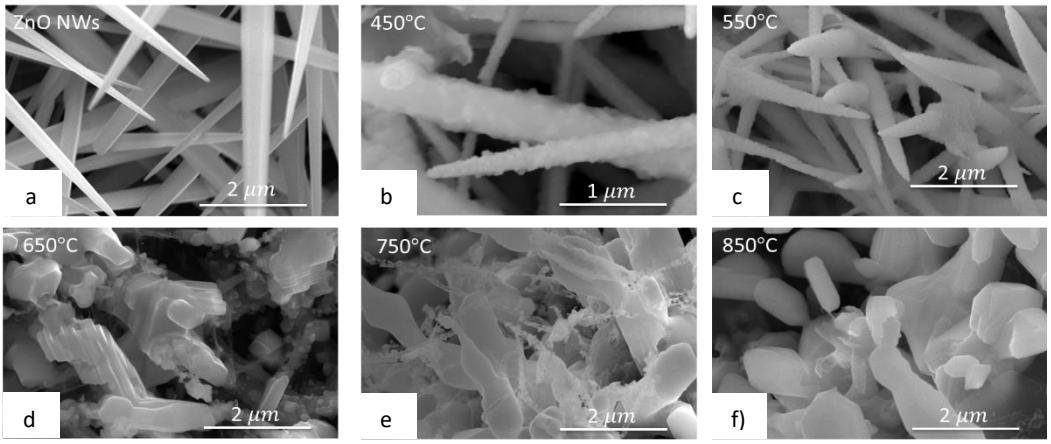

Figure 7: SEM images of a) ZNO NWs, b) ZnO-MoS_2 annealed at 450°C, c) ZnO-MoS_2 annealed at 550°C, d) ZnO-MoS_2 annealed at 650°C, e) ZnO-MoS_2 annealed at 750°C, f) ZnO-MoS_2 annealed at 850°C

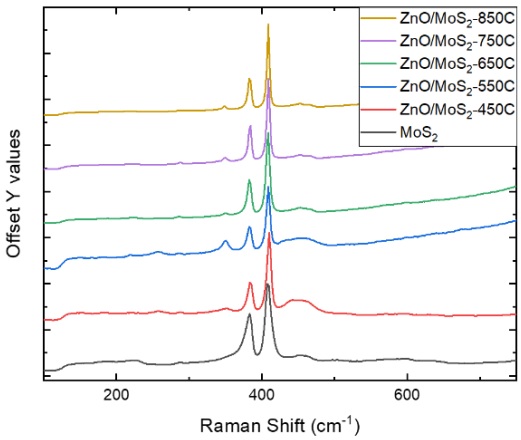

Figure 8: Raman Spectroscopy of ZnO-MoS_2 at various annealing temperatures

Figure 7 shows the SEM images of the synthesis steps to synthesize the CP/CT substrates. As it can be seen in Figure 7b, the ZnO NWs are densely packed and are uniformly distributed. These NWs possess a high aspect ratio with diameters in the hundreds of nanometers and lengths of several micrometers. Figure 7b/c demonstrates that following anneals at 450°C and 550°C the nanowires structure is retained. Above these temperatures, the nanowire morphology is lost as seen in Figure 7d-f. In addition to the loss of morphology, a mass loss was also measured via differential scanning calorimetry around 550°C. However, when analyzed via Raman spectroscopy, it was discovered that ZnS was forming due to the sulfurization process during annealing, as seen in Figure 8.

To reduce the presence of ZnS, further annealings were performed, this time without elemental sulfur present in the furnace. This yielded a significant reduction in the amount of ZnS present as measured via Raman while retaining the nanowire morphology. To further remove any trace ZnO, chemical etchings were done in 0.1 M and 0.01M HCl for various times as can be seen in Figure 9.

As can be seen from Figure 9, the nanowire morphology was maintained. However, upon further Raman and Energy Dispersive Spectroscopy (EDS), we found there was still some presence of Zn species. However, due to the penetration depth of the EDS and Raman, it is difficult to determine where that signal is coming from. One possible theory is that the Zn species signal is coming from the base of the nanowire as well as any that is left-over from coating the carbon paper strands during the first process. To determine this, we are hoping to follow up these studies with transmission electron microscopy in order to isolate and study just the remaining nanowire structure. Following this, we will wrap this study up with polarization sweeps to determine the HER efficacy of the synthesized nanowires.

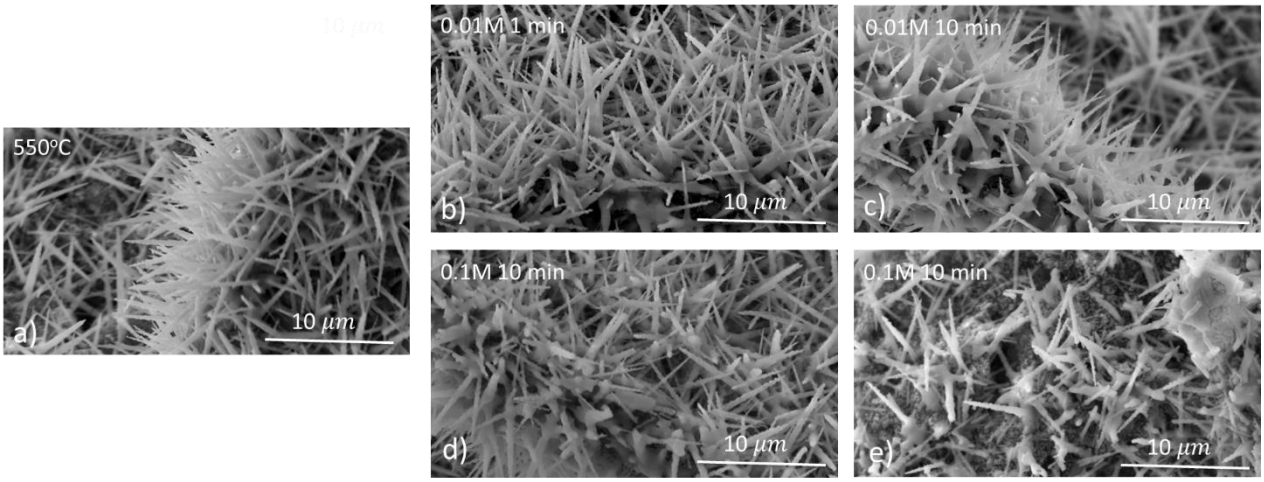

Figure 9: SEM images of a) un-etched NWs, b) 0.01 M for 1 minute, c) 0.01 M for 10 minutes, d) 0.1 M for 1 minute, and e) 0.1 M for 10 minutes

Conclusions

This study developed a facile and scalable electrodeposition technique and annealing methods for catalytically active CoS_x/MoS_2. These catalysts are extremely active for HER in acidic conditions and one of the best performances in alkaline conditions, with overpotentials to reach 10 mA/cm^2 of 112 mV and 60 mV and with Tafel slopes of 113 mV/dec and 81 mV/dec, respectively. The 75-75 exhibited excellent stability in both acidic and alkaline conditions and performed superior to all other samples. This has been attributed to the synergistic properties evolving through the intimate growth of alloys between Co and Mo sulfides, such as better charge transfer and facilitating the adsorption-desorption of hydrogen at the interface of the electrode/electrolyte, as well as increased nano-interfaces between the CoS_x and MoS_2 features. In addition, an unusual morphology was found in the 75-75 catalysts that has not been reported on before. Overall, these scalable catalysts are some of the highest performing HER catalysts while remaining noble-metal free.

The synthesized MoS_2 nanowires are a promising study into developing the first freestanding MoS_2 nanowires. These materials will serve as an excellent catalyst for HER and allow the generation of hydrogen in an efficient and cost-effective manner. Additionally, ZnS/MoS_2 interfaces have interesting properties for photocatalysts due to increasing the photoelectron-hole pair when under illumination. Overall, the nanowire geometry is a promising candidate for replacing expensive, Pt-group materials for HER by allowing for scalable, low-cost synthesis.

References

1. NASA Strategic Plan 2018, pp. 19–21
2. Tsao, J., Lewis, N., et al. US Dep. Energy 1–24 (2006).
3. Anderson, T. R., Hawkins, E., et al. Endeavour (2016) doi:10.1016/j.endeavour.2016.07.002.
4. Turner, J. A. Science (2004) doi:10.1126/science.1103197.
5. Dubouis, N. & Grimaud, A. Chem. Sci. (2019) doi:10.1039/c9sc03831k.
6. Walter, M. G., Warren, E. L., et al. Chem. Rev. **110**, 6446–6473 (2010).
7. Stubbert, B. D., Dasgupta, S., et al. in ACS National Meeting Book of Abstracts (2010). doi:10.1038/nchem.141.
8. Vesborg, P. C. K. & Jaramillo, T. F. RSC Advances (2012) doi:10.1039/c2ra20839c.
9. Morales-Guio, C. G. & Hu, X. Acc. Chem. Res. (2014) doi:10.1021/ar5002022.
10. Tran, P. D., Tran, T. V., et al. Nat. Mater. **15**, 640–646 (2016).
11. Shi, Y. & Zhang, B. Chemical Society Reviews (2016) doi:10.1039/c5cs00434a.
12. Chen, W. F., Muckerman, J. T., et al. Chem. Commun. (2013) doi:10.1039/c3cc44076a.
13. Jakob Kibsgaard, Zhebo Chen, et al. Nature Materials (2012).
14. Wang, H., Lu, Z., et al. Proc. Natl. Acad. Sci. U. S. A. (2013) doi:10.1073/pnas.1316792110.
15. Merki, D., Fierro, S., et al. Chem. Sci. **2**, 1262–1267 (2011).
16. Benck, J. D., Chen, Z., et al. ACS Catal. **2**, 1916–1923 (2012).
17. Lukowski, M. A., Daniel, A. S., et al. J. Am. Chem. Soc. **135**, 10274–10277 (2013).
18. Voiry, D., Yamaguchi, H., et al. Nat. Mater. (2013) doi:10.1038/nmat3700.

19. Popczun, E. J., McKone, J. R., et al. J. Am. Chem. Soc. (2013) doi:10.1021/ja403440e.
20. Popczun, E. J., Read, C. G., et al. Angew. Chemie - Int. Ed. (2014) doi:10.1002/anie.201402646.
21. Sun, Y., Liu, C., et al. J. Am. Chem. Soc. (2013) doi:10.1021/ja4094764.
22. Wei, Y., Zhang, X., et al. Electrochim. Acta (2019) doi:10.1016/j.electacta.2018.12.019.
23. Li, G., Zhang, D., et al. J. Am. Chem. Soc. (2016) doi:10.1021/jacs.6b05940.
24. Ambrosi, A. & Pumera, M. ACS Catal. **6**, 3985–3993 (2016).
25. Murugesan, S., Akkineni, A., et al. ACS Nano **7**, 8199–8205 (2013).
26. Gao, M. R., Chan, M. K. Y., et al. Nat. Commun. **6**, (2015).
27. Jin, Q., Liu, N., et al. Adv. Energy Mater. **10**, 1–12 (2020).
28. Kong, D., Wang, H., et al. Nano Lett. (2013) doi:10.1021/nl400258t.
29. Yang, L., Hong, H., et al. ACS Nano (2015) doi:10.1021/acsnano.5b02188.
30. Li, Y., Wang, H., et al. J. Am. Chem. Soc. **133**, 7296–7299 (2011).
31. Lin, S. H. & Kuo, J. L. Phys. Chem. Chem. Phys. (2015) doi:10.1039/c5cp04760a.
32. Lee, J., Kang, S., et al. J. Phys. Chem. Lett. (2018) doi:10.1021/acs.jpclett.8b00712.
33. Xie, J., Zhang, H., et al. Adv. Mater. (2013) doi:10.1002/adma.201302685.
34. Lin, L., Miao, N., et al. ACS Nano (2016) doi:10.1021/acsnano.6b04904.
35. Ye, G., Gong, Y., et al. Nano Lett. (2016) doi:10.1021/acs.nanolett.5b04331.
36. Li, H., Tsai, C., et al. Nat. Mater. (2016) doi:10.1038/nmat4465.
37. Zhong, W., Wang, Z., et al. Angew. Chemie - Int. Ed. **59**, 22743–22748 (2020).
38. Oyedele, A. D., Yang, S., et al. J. Am. Chem. Soc. **139**, 14090–14097 (2017).
39. Wang, Z., Lin, Z., et al. Adv. Energy Mater. **11**, 7–13 (2021).
40. Huang, S., Meng, Y., et al. Adv. Funct. Mater. **27**, 1–10 (2017).
41. Guan, C., Liu, X., et al. Nanoscale Horizons **2**, 342–348 (2017).
42. Souleymen, R., Wang, Z., et al. J. Mater. Chem. A **6**, 7592–7607 (2018).
43. Ma, X., Zhang, W., et al. Nanoscale **10**, 4816–4824 (2018).
44. Bonde, J., Moses, P. G., et al. Faraday Discuss. (2008) doi:10.1039/b803857k.
45. Zhou, X., Yang, X., et al. Nano Energy (2017) doi:10.1016/j.nanoen.2017.01.011.
46. Yan, K. L., Qin, J. F., et al. Chem. Eng. J. (2018) doi:10.1016/j.cej.2017.10.074.
47. Zhang, N., Gan, S., et al. ACS Appl. Mater. Interfaces **7**, 12193–12202 (2015).
48. Yan, Y., Xia, B., et al. J. Mater. Chem. A **3**, 131–135 (2015).
49. Nikam, R. D., Lu, A. Y., et al. ACS Appl. Mater. Interfaces **7**, 23328–23335 (2015).
50. Levinas, R., Tsyntsaru, N., et al. Electrochim. Acta **317**, 427–436 (2019).
51. Podlaha, E. J. & Landolt, D. J. Electrochem. Soc. **144**, 1672–1680 (1997).
52. Sun, P., Zhang, W., et al. J. Mater. Chem. A **2**, 3498–3504 (2014).
53. Geller, S. Acta Crystallogr. **15**, 1195–1198 (1962).
54. Nowack, E., Schwarzenbach, D., et al. Acta Crystallogr. Sect. B **47**, 650–659 (1991).
55. Liang, L. & Meunier, V. Nanoscale **6**, 5394–5401 (2014).
56. Lyapin, S. G., Utyuzh, A. N., et al. J. Phys. Condens. Matter **26**, 1–6 (2014).
57. Wang, H., Lu, S., et al. J. Mater. Chem. A **3**, 23677–23683 (2015).
58. Dai, X., Du, K., et al. ACS Appl.

Mater. Interfaces **7**, 27242–27253 (2015).
59. Kendall, L., Chamaani, A., et al. ACS Appl. Energy Mater. **4**, 13676–13683 (2021).
60. Asadi, M., Kumar, B., et al. ACS Nano **10**, 2167–2175 (2016).
61. Yan, Y., Ge, X., et al. Nanoscale (2013) doi:10.1039/c3nr02994h.
62. Shit, S., Chhetri, S., et al. ChemElectroChem **6**, 430–438 (2019).
63. Senthil, R. A., Wang, Y., et al. Int. J. Hydrogen Energy **44**, 16537–16547 (2019).
64. Mahmood, N., Yao, Y., et al. Adv. Sci. **5**, (2018).
65. Wang, J., Zhong, H. X., et al. ACS Nano **10**, 2342–2348 (2016).
66. Feng, L. L., Fan, M., et al. J. Mater. Chem. A **4**, 6860–6867 (2016).
67. Bose, R., Jin, Z., et al. Langmuir **33**, 5628–5635 (2017).
68. Kornienko, N., Resasco, J., et al. J. Am. Chem. Soc. **137**, 7448–7455 (2015).
69. Zhu, H., Zhang, J., et al. Adv. Mater. **27**, 4752–4759 (2015).
70. Wang, P., Wan, L., et al. Int. J. Hydrogen Energy **44**, 16566–16574 (2019).
71. Zhang, N., Ma, W., et al. Int. J. Hydrogen Energy **41**, 3811–3819 (2016).